**Tuning the stator subunit of the flagellar motor with coiled-coil engineering.**

Pietro Ridone[1], Daniel L. Winter[1], Matthew A. B. Baker[1]

1. School of Biotechnology and Biomolecular Science, UNSW Sydney, Australia.

**Abstract:**
Many bacteria swim driven by an extracellular filament rotated by the bacterial flagellar motor. This motor is powered by the stator complex, MotA5MotB2, a heterodimeric complex which forms an ion channel which couples energy from the ion motive force to torque generation. Recent structural work revealed that stator complex consists of a ring of five MotAs which rotate around a central dimer of MotBs. Transmembrane (TM) domains TM3 and TM4 from MotA combine with the single TM domain from MotB to form two separate ion channels in this complex. Much is known about the ion binding site and specificity, however to-date no modelling has been undertaken to explore the MotB-MotB dimer stability and the role of MotB mobility during rotation. Here we modelled the central MotB dimer using coiled-coil engineering and modelling principles and calculated free energies (BUDE) to identify stable states in the operating cycle of the stator. We found 3 stable coiled-coil states with interface angles 28°, 56° and 64°. We tested the effect of strategic mutagenesis on the comparative energy of the states and correlated motility with a specific hierarchy of stability between the three states. In general, our results indicate agreement with existing models describing a 36˚ rotation step of the MotA pentameric ring during the power stroke and provide an energetic basis for the coordinated rotation of the central MotB dimer based on coiled-coil modelling.

**Introduction:**

The bacterial flagellar motor (BFM) is a complex nanoscale engine that converts ion flux into the rotation of a flagellum to propel bacteria through their surroundings[1,2]. A crucial component of this complex is the stator subunit which is responsible for the torque-generating step of the motor[3,4]. In *E. coli,* the stator subunit is in fact composed of two transmembrane (TM) proteins (MotA and MotB) which assemble around the basal rotor of the flagellar motor and form a proton channel at their interface[5]. The inward flux of ions across the complex is efficiently coupled to a mechanical stimulus applied onto the rotor protein FliG which ultimately drives the rotation of a single flagellum[6].

The structure of the full $MotA_5MotB_2$ complex was solved in 2020[7,8] revealing that the stator complex likely acted as a rotary motor itself. Further recent structural work has identified the basis for ion selectivity and many catalytic residues involved in the process[9]. The current consensus model is that a transmembrane pentameric ring of MotA subunits rotates around a central dimer stalk of MotB TM domains[9,10]. The model details the conformational waypoints through which the MotA subunit passes during the gating cycle of the stator, but our understanding of the dynamics, in general, is limited, and in particularly for the MotB subunit central stalk.

The central MotB dimer is important because it harbours the catalytic centre. It has been proposed to rotate in place between protonated and non-protonated states[10]. Previous work suggested that the MotB TM domains exchange their interface contacts during gating and may pivot along their helical axis[11], in a similar fashion to the proposed mechanism for the homologous TolR protein[12]. The dimerization of MotB at the TM domain was shown to be essential for motility as modifications to TM residues that restrict or alter the conformational space of the dimer e.g. cysteine crosslinking and tryptophan-scanning mutagenesis, generally diminished motility[11,12].

The MotB stalk appears to assemble as a dimeric parallel coiled-coil in recently published structures[7,8]. Coiled-coils are well-characterized structural motifs where alpha-helices interact to form dimers or higher order oligomeric states[13]. A repeating seven residues-long "heptad" motif with alternating hydrophobic (*h*) and polar (*p*) residues forming the general pattern *hpphppp* along the alpha-helices results in a core interface where the hydrophobic residues engage in knob-into-hole (KIH) interactions. The sequence-structure relationship of coiled-coils is well understood and design principles have been established to create synthetic coiled-coils. Dimers are a specific example: it has been shown that isoleucine and leucine in positions *a* and *d* of a repeating heptad *abcdefg* (corresponding to the pattern *hpphppp*) greatly favor dimerization over other oligomeric states, whereas isoleucine at both positions favors trimers[14]. Moreover, the structure of coiled-coils can be parametrically modelled, which greatly accelerates the calculation of their physical properties, such as interaction strengths[15]. Parametric modelling entails the use of very few parameters (the radius, interface angle, and pitch of a coiled-coil) to describe the entire backbone structure. Parametric modelling, in combination with the BUFF forcefield from BUDE (Bristol University Docking Engine)[16] has been successfully applied to predict the structures of natural and synthetic coiled-coils[17,18].

In this study, we investigated the dimerization interface of MotB using parametric modelling to represent the MotB dimer as a dynamic coiled-coil. This simplification of the MotB structure enables the rapid calculation of the total energy of the system to discriminate between stable and unstable conformations. From these results, we rationally designed stator sequence variants to be tested *in vivo* and to better understand how MotB dimer stability may relate to overall conformational dynamics of the stator complex during its gating cycle.

In this study, we investigated the dimerization interface of MotB using parametric modelling to represent the MotB dimer as a dynamic coiled-coil. This simplification of the MotB structure enables the rapid calculation of the total energy of the system to discriminate between stable and unstable conformations. From these results, we rationally designed stator sequence variants to be tested in vivo and to better understand how MotB dimer stability may relate to the conformational dynamics of the stator complex during its gating cycle. By testing the motility of the predicted stable and unstable conformational states for each MotB variant tested in vivo, we aimed to identify which coiled-coil configurations were correlated with motility, and to inform the conformational changes undertaken by EcMotB, and its extant homologs, during their gating cycle.

**Results**

We modelled the *Ec*MotB TM domain as a parallel coiled-coil based on the most recent structures of MotB from *B. subtilis* (PDBID: 6YSL), *C. sporogenes* (PDBID: 6YSF) and *C. jejuni* (PDBID: 6YKM)[7,8] (Fig. 1). A set of ISAMBARD models of the 20-residue long *Ec*MotB peptide IAYA**D**FMTAMMAFFLVMWLI (corresponding to residues 28-47 of WT *Ec*MotB; the catalytic residue D32 is indicated in bold) with varying interface angles were aligned to the crystal structures to formally identify the "register" of the MotB coiled-coil, that is, what positions in the coiled-coil heptad each residue occupies. Based on RMSD calculations and the orientation of the catalytic aspartate (D32), we established that the 20-residue long MotB dimer stalk is best described as a coiled-coil starting at position *e*. In other words, residues A31, M34, M38, F41, and W45 occupy positions *a* and *d* along the coiled-coil, forming the core interface. These results agree with previous reports where mutation of these residues to cysteine led to crosslinking between the two MotB subunits, indicating proximity[19]. Further analysis using CCBuilder of the peptide IAYADFMTAMMAFFLVMWLI as a parallel dimeric coiled-coil starting at position *e* indicated that the five core residues could form KIH interactions.

In light of these results, we decided to model MotB as a dimeric coiled to inform our *in vivo* mutagenesis experiments. To this end, rather than simply considering the most stable conformation calculated by ISAMBARD, we considered the conformational space of MotB by generating coiled-coil structural models with varying interface angles and radii and then, for each combination of the two parameter values, calculating the total energy of the system using the BUDE forcefield. This *in silico* conformational screen revealed the potential existence of 'stability wells' (more stable configurations) and 'forbidden states' (unstable configurations) for the WT *Ec*MotB (Fig. 2A). Interestingly, the deepest 'stability well' (#4, Fig. 2B) did not correspond to the configuration adopted in the cryo-EM structures (#1, Fig. 2B).

Next, we considered strategic point mutation of coiled-coils to investigate if the stability of the MotB dimer would change after replacing the key *a* and *d* residues forming the core interface. We considered the design rules of synthetic coiled-coils and hypothesised that alanine mutations would systematically weaken the coiled-coil interaction by disrupting the hydrophobic KIH interactions, whereas isoleucine and leucine mutations would lead to more stable KIH interactions and thus a more stable coiled-coil (when isoleucine and leucine occupy positions *a* and *d*) or to steric clashes (when isoleucine occupies both positions *a* and *d*). Therefore, core residues were systematically mutated *in silico* to alanine, isoleucine, or leucine at positions *a* and *d* in over 200 permutations (see Method and Supplementary Table 1). In addition, we also considered the M38G mutation that appeared to disrupt KIH interactions in CCBuilder analyses. In total, a library of 221 sequence variants was generated *in silico*.

To test the above hypothesis *in silico*, we repeated the conformational analysis using ISAMBARD for each MotB variant modelled as a coiled-coil and compared the energy landscape of each sequence variant to the WT sequence. Different mutations resulted in a shift of the "stability wells" towards different interface angles and radii values and, in some extreme cases, to the absence of stability wells. Altogether, the results indicate that the selected mutations in the core of the MotB dimerization interface could affect its accessible conformational space and, presumably, affect cell motility. Further to this analysis, the three-dimensional (3D) BUDE energy landscapes were collapsed into two-dimensional (2D) energy profiles by averaging the energy values for radii between 4 to 5 Å (Fig. 2C). This range of radii values in BUDE encompassed the radii observed in the reference structures (4.7 to 4.9 Å) and contained most of the 'stability wells' and 'forbidden states' of interest to compare sequence variants. In these dimensionally reduced datasets, we subsequently considered the interface angle parameter as the main variable affecting the energy of the coiled-coil system. Varying the interface angle means rotating the two MotB alpha-helices relative to each other, shifting the orientation of the core interface residues. This type of rotation is known as a register shift, as the interface angle is related to the coiled-coil register, and register shifts have been shown elsewhere to underpin biological processes such as dynein recruitment[20,21] and the activity of proteasomal ATPase[22].

We next sought to select a subset of mutants to verify whether the differences in calculated energy profiles for MotB sequence variants correlated with BFM activity. Comparison of the 2D BUDE energy profiles suggested that single mutations could be sufficient to alter the accessible conformational space of MotB, and therefore affect cell motility (Fig. 2C, 2D). We selected 9 single mutants (SI Fig. 1) and an additional 10 double mutants and 4 triple mutants (SI Fig. 2) that showed varied energy profiles for *in vivo* experimentation. We restricted our *in vivo* testing to variants displaying alanine and/or isoleucine replacements.

We recombinantly expressed the selected sequence variants of MotB in an *E. coli* Δ*motAB* background strain and assessed the motility of bacteria on swim plates (Fig. 3A) and at a single cell level (Fig. 3B). Some of the single point mutations affected the size of swim rings (M34A, M34I, M38A, F41A) whereas all other mutations, including the selected double and triple mutants, abolished motility (Supplementary Fig. 3). Amongst the motile mutants, the first two

had a comparable (M34A) or markedly positive (M34I) effect on motility, while M38A and F41A decreased the size of the swim rings (Fig.3A). Motility was confirmed at the single cell level when these four variants were tested in tunnel slides. Tethered cell assay measurement of cell speed revealed a significant reduction in cell speed for all the motile variants including M34I ($p < 0.001$, T test) (Fig. 3B). The M34I variant was also found to have a significant decrease in CW Bias ($p < 0.05$) when compared to M34A indicating an increased propensity for CCW motor runs over tumbles (Supplementary Fig. 4), which may explain the increased size of swim rings for this variant. Interestingly, M34I was able to swim in higher density agar (0.4%) better than WT or any other variant, suggesting a change in torque generation in the mutant stator (SI Fig. 5).

A comparison of the mean 2D BUDE profiles of all motile and non-motile variants suggested that the stability of the coiled-coil around the interface angle of 28°, where M34 plays a key role in KIH interaction, was crucial for function (Fig. 3C). The influence on the total energy from mutation at that site, adjacent to the catalytic Aspartate residue (D32), appears to be correlated with a motile phenotype. When comparing the 2D BUDE profiles of each MotB variant tested *in vivo*, we noticed a similarity in the shapes of the BUDE profiles of the motile variants, whereas the profiles of the non-motile variants diverged substantially (Fig. 3D). Aligning the profiles with respect to their peak values ($BUDE^{max}$) revealed more differences between motile and non-motile profiles than the strength of interaction at the 28° configuration alone. The BUDE gap between the minimum value of each profile and the peak corresponding to the 44° configuration appeared to be similar across the motile variants.

Further comparison of the 2D profiles of all point mutants suggested a pattern of specific interface angles, or configurations, associated with motility ( SI Fig. 6). All the *Ec*MotB variants found to be motile had the 66° (cross), 28° (square), 56° (circle) and 44° (triangle) configurations in ascending order of magnitude. The exceptions to this pattern were the single mutants A31I, F41I and M38G, which featured destabilized 44°, 28° and 28° configurations respectively and the double mutants A31I M34I and A31I M38A featuring a destabilized 44° configuration. This indicated that the relative stability of the 28°, 56° and 64° configuration play a role in determining the function of MotB and that this pattern may reflect the order of configurations undertaken by WT MotB during its gating.

We captured the features associated with motility variants by defining two metrics, *f1* and *f2* (Fig. 2E), where $f1 = BUDE^{56^\circ} - BUDE^{28^\circ}$ and $f2 = BUDE^{min} - BUDE^{max}$ (Fig. 3E). The first parameter, *f1*, is the BUDE energy gap at an interface angle of 28°, associated with motile variants (Fig. 3C), and the reference interface angle of 56°, predicted to form a KIH interaction with the conserved residue F41 (Fig. 2B, 'circle' config). Residue F41 appeared to have the more consistent value across the profiles of all variants (SI Fig. 7 ). With *f2* we measured the energy gap between the minimum and maximum BUDE values across the profile, or the energy barrier separating the stability wells. Separating all variants on the basis of these two parameters revealed a cluster of optimal *f1* and *f2* values for the motile variants of *E. coli* MotB (Fig. 3F). These results suggest that a combination of energetic parameters contained within the 2D profiles could be descriptive of functional *Ec*MotB variants and that the relative stability of each hotspot configuration needs to be maintained to operate the *E. coli* stator.

We also searched for other metrics that could cluster and separate motile and non-motile sequences to facilitate the prediction of motile variants of *Ec*MotB from their 2D profile models. We defined *f3* = $[(BUDE^{56^\circ} - BUDE^{28^\circ}) - (\Delta BUDE^{56^\circ} - \Delta BUDE^{28^\circ})]$ and observed that this was correlated with motility only when yielding a positive value, where ΔBUDE is the difference in BUDE energy between the mutant and WT MotB at the given interface angle. Additionally, we defined *f4* = $(BUDE^{min} - BUDE^{max} – BUDE^{max}) = (BUDE^{min} - 2*BUDE^{max})$, which considered not only the range of the profile but also its overall magnitude, and was found to correlate with motility only when resulting in a positive value. The ability to form KIH interactions and the satisfaction of these 2 parameters, *f3* > 0 and *f4* > 0, were specifically matching only the functional variants of *E. coli* MotB amongst the ones studied here (Supplementary Fig. 8 ).

To explore a larger set of TM sequences associated with motile bacteria we examined homologues of MotB. We generated a 91 member phylogeny of MotB using RAxML[23] across diverse clades and simultaneously calculated the BUDE energy for MotB across each of the 91 bacterial species (Fig. 4A, SI Fig. 9, 10). To determine whether our observations were applicable to other extant homologs we carried out the same BUDE analysis on 70 representative homologous sequences across the phylogeny (Supplementary Fig. 9A, 10) and produced a 2D BUDE profile of each 20 amino acid-long parallel coiled-coil TM domain (SI Fig. 9B). To examine clustering and compare with the phylogenetic clustering, we translated each BUDE plot relative to its $BUDE^{max}$ value (Fig. 4B, ). These appeared to cluster in 7 distinct groups (Fig. 4C), matching phylogenetic clades (Fig. 4A), and each displaying one or more conserved amino acid residues amongst the representative positions *a* and *d* of their heptad repeats, evidenced by their consensus logos (Fig. 4C). These clusters appeared to concentrate around specific *f1* and *f2* value ranges when plotted on a graph (Fig. 4D). Out of these 70 sequences, 66 were found to have *f1* > 0, while only a subset had *f2* > 0 (SI Fig. 9C ). Clusters were separated by the identity of their residue 38 (position *a*) and shared the conserved D32 and F41 (*d*) residues. Positions 31 (*a*), 34 (*d*) and 45 (*a*) also displayed unique residues in specific clusters (Fig. 4A, 4C).

## Discussion

In this study we constructed several stator variants, designed *in silico* according to coiled-coil design principles, and measured their capacity to drive swimming *in vivo* in *E. coli*. Because the residues targeted by mutagenesis were at the hydrophobic interface of the coiled-coil structure we assumed that the effects of amino acid replacement would be confined to MotB and its dimerization, with negligible effects on the surrounding MotA. We envisioned the disruption of function in MotB as the result of preventing the assembly of the coiled-coil via knobs-in-holes, the stabilization of the coil in a non-functional configuration or the inability of the stator to shift between configurations.

We tested a mutant with the intent to disrupt motility (M38G), by disrupting the KIH interactions between the coils. A gain-of-function variant (M34I), designed to have a stronger coiled-coil interaction, demonstrated that coiled-coil stability could be linked to improved motility, but we also observed that 'tightening' the coiled-coil at the wrong knob could disrupt function entirely. For example, increasing the BUDE interaction in the central knob (M38I mutant) was predicted to stabilize the 64° conformation. Instead, this yielded a non-motile variant. In contrast, the BUDE model indicated M34I to be the only isoleucine mutant with increased dimer stability within the coiled-coil of all of the hotspot configurations. The reason for improved swimming of this variant on swim plates remains unclear because the motor performance appeared to be reduced compared to WT in single-cell assays (both in tethered and free-swimming assays). In single-cell assays, M34I was indistinguishable from the M34A variant, while M34A displayed WT phenotype on swim plates in contrast to M34I.

Swimming of M34I, WT, M34A, M38A and F41A correlated with shared properties of their BUDE profiles. Although a bulk comparison of our motile and non-motile variants showed a difference in their BUDE magnitude at a specific hotspot on the profile (the 28° configuration) we sought to identify other features in the BUDE profile to use for classifying motile and non-motile classes. We defined two parameters, *f1* and *f2,* to differentiate between classes and the effect of each of point mutant on motility. In this framework, M38A maintains the profile shape; M38I reduces $BUDE^{max}$ and abolishes function; F41A destabilizes the 56° configuration, maintaining a positive *f1* and therefore a functional stator, while F41I stabilizes it and abolishes function by lowering *f1* below zero; W45A increases $BUDE^{max}$ beyond a functional level and W45I destabilizes the 28°configurations thus lowering *f1* to a negative value. A31I reduces $BUDE^{max}$ compared to WT and abolishes function.

Using *f1* as an indicator of functionality in a stator implies that the interaction is dominated by the knobs at position 34 and the conserved F41. We thus speculate that a transition between these two configurations is essential for the function of the stator. Previous work involving chemical cross-linking between MotB coiled-coil residues suggested that the TM structure is flexible and able to exchange the residues at the CC interface during a rotation of ~36° (*1*). In line with those considerations, we found that BUDE profile features at all four configurations (28°, 44°, 56° and 64° hotspots in *Ec*MotB) were predictive of stator functionality, that is, motility on swim plates.

The *f1* and *f2* parameters were useful also in describing and clustering extant MotBs. Indeed it may be that these clusters represent families of MotB homologs that are related in their functional characteristics. Notably, *V. alginolyticus* PomB and *E. coli* MotB, of which functional chimeras exist[24], belong to the same cluster (green, Fig. 4). These two stators are known to differ in their power source ($Na^+$ and $H^+$ respectively) and differ in the identity of their homologous residue 45 (L45 for $Na^+$, W45 for $H^+$) while showing similar 2D profiles. Another notable cluster is the one shared by *B. subtilis*, *C. sporogenes* and *C. jejuni* (black Fig. 3). These three species are sources of the most detailed cryo-EM structures of the $MotA_5B_2$ stator complex to date. It is possible that these complexes were more stable and thus easier to purify and resolve due to stronger MotB coil interaction than the *E. coli* or *V. alginolyticus* homologs.

We noted a linear relationship between the hydrophobicity of residue 38 with the $BUDE^{max}$ magnitude. MotB clusters displaying F, L or M at position 38 had a proportionally high $BUDE^{max}$ peak in their profiles, with F38 being the highest and M38 the lowest (SI Fig. 9B). The height of this energetic barrier could indicate a required activation energy to drive stator gating, such as protonation at the catalytic aspartate or steric interaction with MotA[9].

Elsewhere we have extensively examined large phylogenies of MotB[25]. Here we calculated a small phylogeny that was representative of wider flagellar diversity to compare how BUDE energetics clustered across a model of evolutionary history. Our MotB classes obtained from clustering similar energetic profiles closely overlap clades from our phylogeny obtained using traditional tree-building approach (Fig. 3A). This suggests that conservation of sequence identity is closely linked to conservation of functional traits, and indeed it is notable that BUDE free energy profiles calculated across only the 20 transmembrane residues so naturally fell into clusters that matched those generated by sequence similarity from phylogenetic consideration across the full length MotB. Together, these results show that cluster-based comparison of BUDE free energies can recapitulate phylogenetic clades, and shows that there is evolutionary evidence for conservation of distinct BUDE stable states. This clustering based on MotB-MotB dimer stability could be further examined in greater detail, for example, with regard to species that have specific high-torque operating environments, eg *Spirochaetes* sp.. These species typically have large rotors to generate larger torques[5,26–28], but there could be signatures of conservation of increased stator stability elsewhere that may correlate with high-torque or viscous operating conditions.

Based on the model proposed by Rieu et al.[10] we describe a model of mechanochemical gating that includes the conformational changes in the MotB TM domain studied here (Fig.5). Our model assumes that the rotation of the MotA pentamer can occur only if both catalytic aspartates in MotB are protonated. We propose that a single protonated aspartate, engaging MotA with MotB, couples the synchronized rotation of both $MotA_5$ and $MotB_2$ by 36° clockwise, and is then released into the cytoplasm after the entry of a second proton binding onto the other disengaged aspartate. In this model, the binding of a proton to MotB is the trigger that mediates the transition from the 28° configuration to the less stable 56° configuration (see *f1* parameter correlating 28° and 56° configs). The engagement of the protonated aspartate with close residues in MotA TM3-4 via hydrogen bonds stabilizes the TM helix of MotB and allows the dimer to complete a 36° rotation counter-clockwise into the

64° configuration ($BUDE^{min}$). At this stage, the unbound aspartate aligns with the periplasmic entry pore where a new proton can bind the disengaged aspartate and destabilize the coil causing a return to the 28° configuration of intermediate BUDE magnitude.

If the 56° configuration were more stable than the 28° configuration, the stator may not be able to complete a 36° CW turn and might stabilize into the 56° configuration and be unable to return to 28˚ to reset for a further cycle. The magnitude of the energetic barrier separating the 28° configuration from the 56° and 64° configurations, represented by $BUDE^{max}$, could be interpreted as the energetic requirement for a proton-binding event to trigger a power stroke. For example, a more hydrophobic KIH at position 38 of the *Ec*MotB, would increase the height of the $BUDE^{max}$ peak and thus the energy barrier (Fig. 4). Future work may interrogate the PMF dependence on this barrier and altering the available energy could rescue motility in MotB variants with increased $BUDE^{max}$.

Whilst the function of the flagellar stator complex clearly depends not only on the pore lining residues between MotA and MotB, and torque-generating interactions between MotA and FliG, our overall conclusion is that it also depends on the degree of interaction between the two TM domains of MotB that assemble as a coiled-coil at the core of the stator. The residues responsible for knob-in-hole interactions at the dimerization interface of *E. coli* MotB, and possibly other extant homologs, appear to tolerate only mutations that do not shift their coiled-coil energetics too far from wild-type. What we learned from this work will improve our ability to engineer mutant MotB's, chimeric stators or synthetic variants of the bacterial flagellar motor.

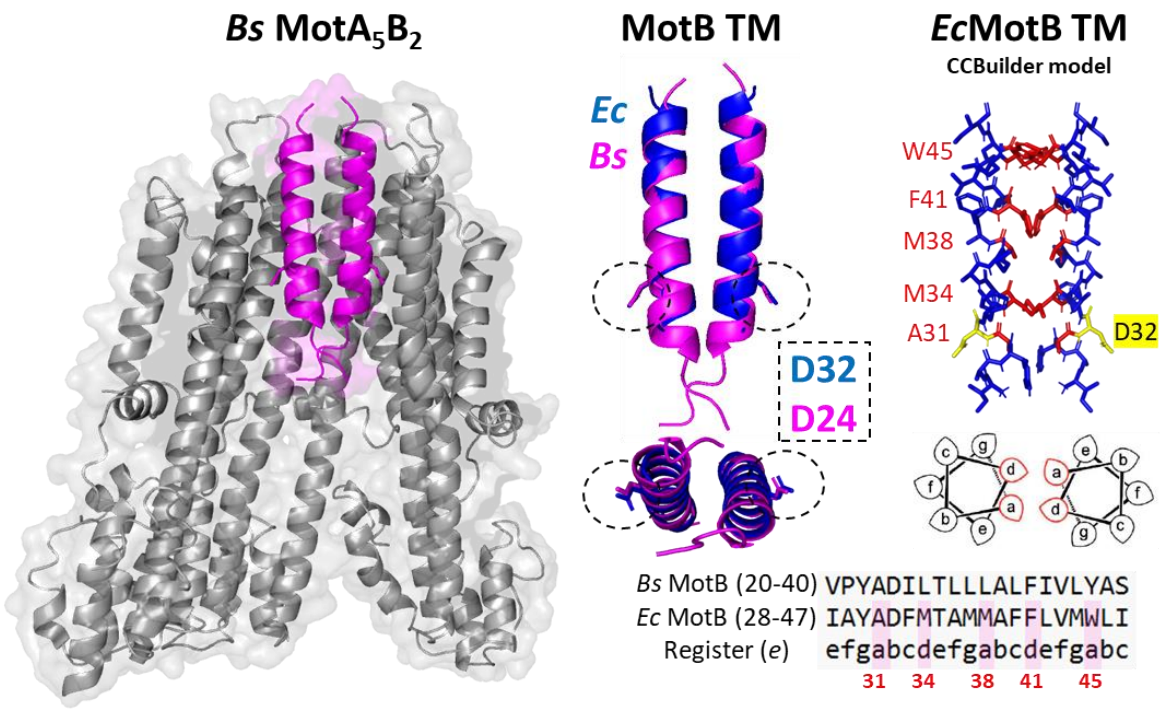


**Figure 1. Modelling the transmembrane domain of MotB as a dimeric coiled-coil**.

The crystal structure of *B.subtilis* $MotA_5B_2$[PDB 6YSL] (left) was used as the starting point for *E.coli* MotB TM modelling. A CCBuilder model of the homologous sequence from *E.coli* was generated (blue) and aligned to the reference *Bs*MotB dimer (purple). A coiled-coil model in the *e* register was selected based on the orientation of the catalytic aspartates D32 (*E.coli*) and D24 (*B.subtilis*) (middle, dotted circles in the side and bottom views of the TM domain). Residues A31, M34, M38, F41 and W45 were found to be at the coiled-coil interface (right), corresponding to positions *a* and *d* of the heptad repeat able to participate in knob-in-kole (KIH) interactions (labelled in red on the atomic model and heptad diagram underneath). An alignment of the two homologous amino acid sequences and the selected register is shown on the bottom-right, with *E.coli* residues at the *a* and *d* positions highlighted in red and numbered.

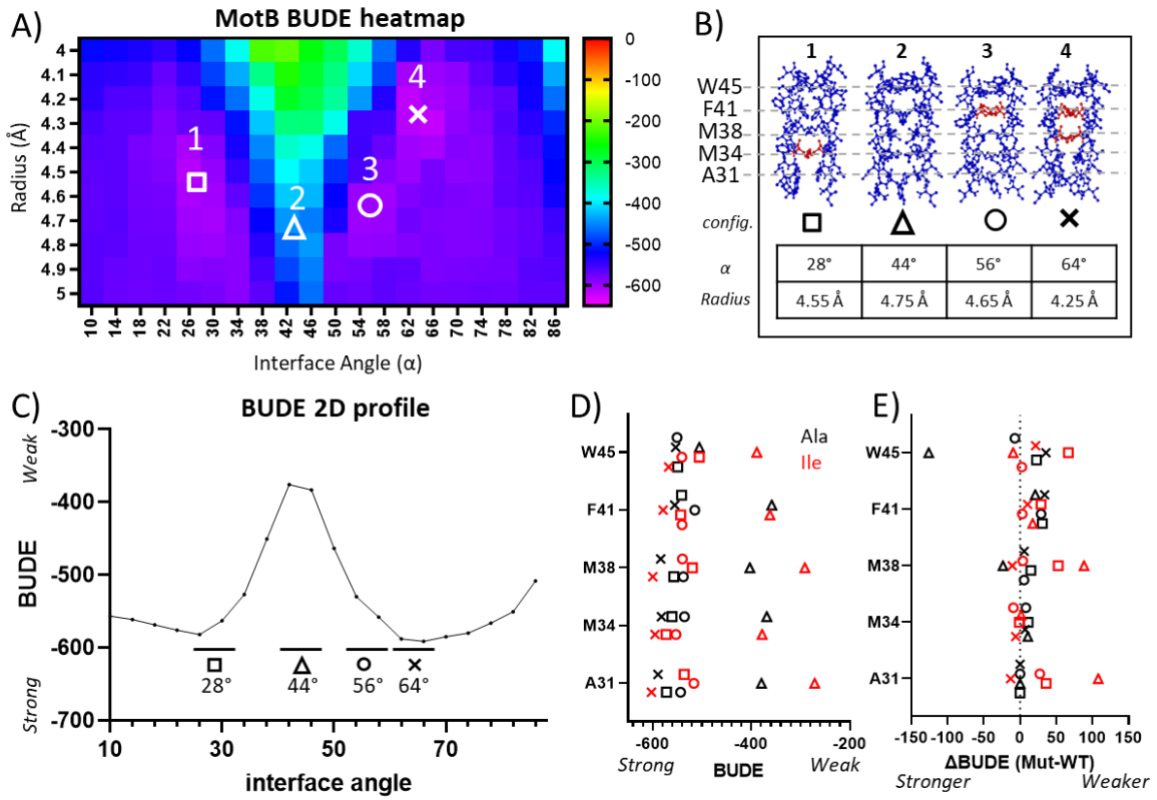


**Figure 2. Characterization of the MotB TM coiled-coil interaction energy.**

A) Heatmap representation of the free energy (BUDE) interaction between the two MotB coils, as a function of radius (y axis) and interface angle (x axis). Four regions, including three stability hotspots and a 'forbidden' configuration, are indicated by symbols and numbered 1-4.

B) Atomic models of the MotB coiled-coil in different configurations of interface angle (α) and radius. The configurations (*config.*) highlighted in A are shown and labelled with their respective symbols. The main amino acid residue responsible for KIH interactions are labelled in red on each model.

C) Two-dimensional representation of the BUDE heatmap shown in B. Four symbols are used to indicate the angle coordinates of the hotspots shown in B and C. The BUDE value calculated at interface angles 28°, 44° 56° and 64° is calculated as the average of the two neighbouring data points above the black horizontal bars.

D) Plot of predicted BUDE energy changes at each of the four hotspots (symbols) after amino acid replacement at positions *a* and *d* of the MotB coil with amino acids alanine (Ala, black) or isoleucine (Ile, red).

E) Net difference in predicted BUDE between WT and mutant MotB sequences at each of the four hotspots (ΔBUDE). Left-shifted (< 0) values are associated with increased stability of the CC, while right-shifted ( > 0) indicated a weaker CC interaction for each configuration.

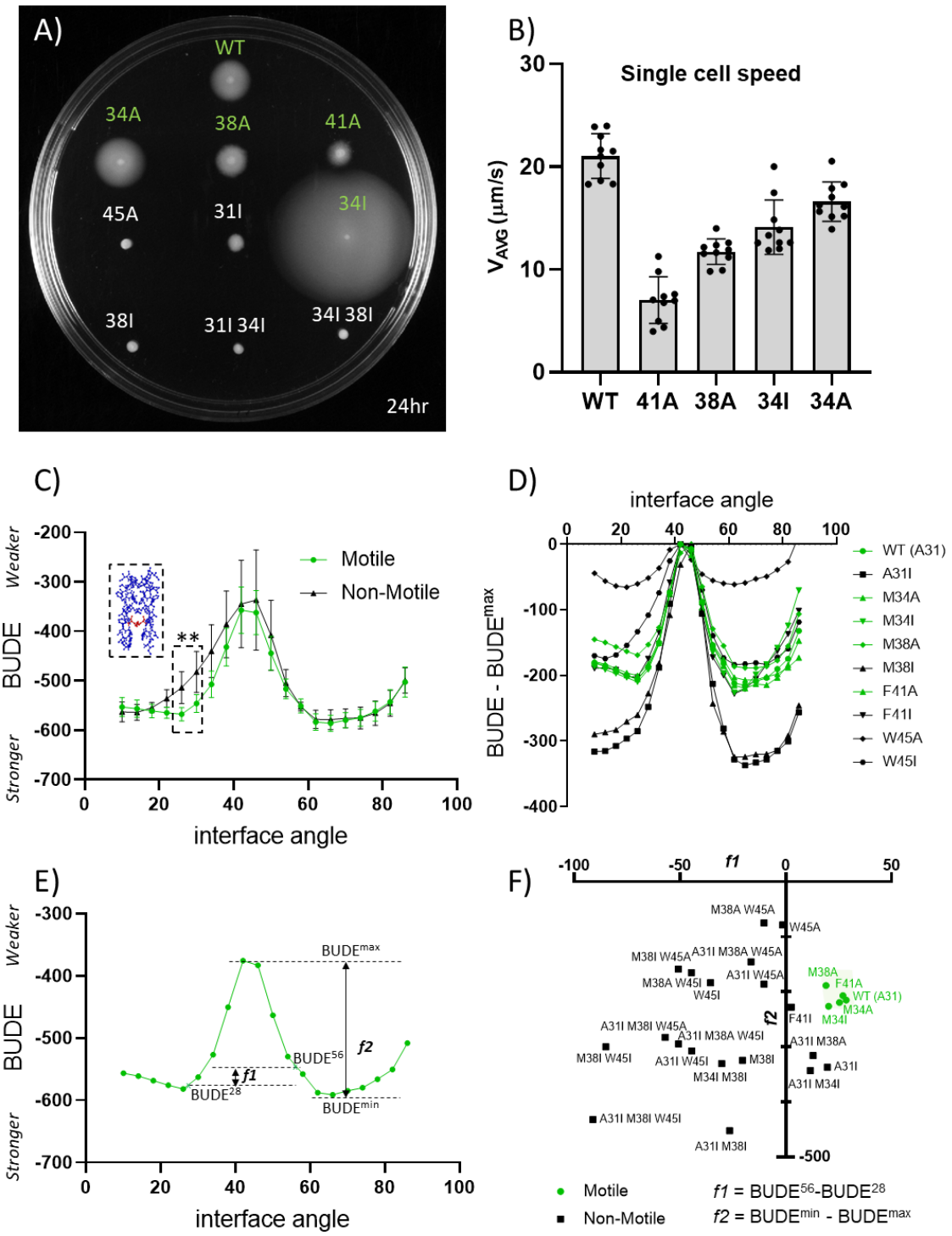


**Figure 3. Testing coiled-coil variants in *E.coli* and parametrization of 2D BUDE profiles.**

A) Swim plate assay of *E. coli* ΔMotAB + pDB108 expressing WT MotA and either WT (top) or mutant MotB's on LB agar 0.3% supplied with 0.1 % arabinose and Chloramphenicol after 24 hr incubation at 30'C. See supplementary figure X for all variants tested in this study.

B) Single *E. coli* cell swimming speed measured in motility buffer. The 10 fastest cells for each mutant are plotted here. Bars indicate Mean speed (µm/s) + SD.

C) Average 2D BUDE plots of motile (green) vs non-motile (black) MotB variants. The Knob-in-hole configuration adopted by MotB in the 28° configuration is highlighted in the dashed box. Bars indicate Mean + SD.
D) Individual 2D BUDE plots of motile (green) vs non-motile (black) MotB variants, translated according to their respective $BUDE^{max}$ values.
E) Graphical representation of the *f1* and *f2* parameters visualized on the 2D BUDE profile of *E. coli* WT MotB.
F) Individual variants mapped on an XY graph where X = *f1* and Y = *f2*. The green box indicates a cluster of motile variants.

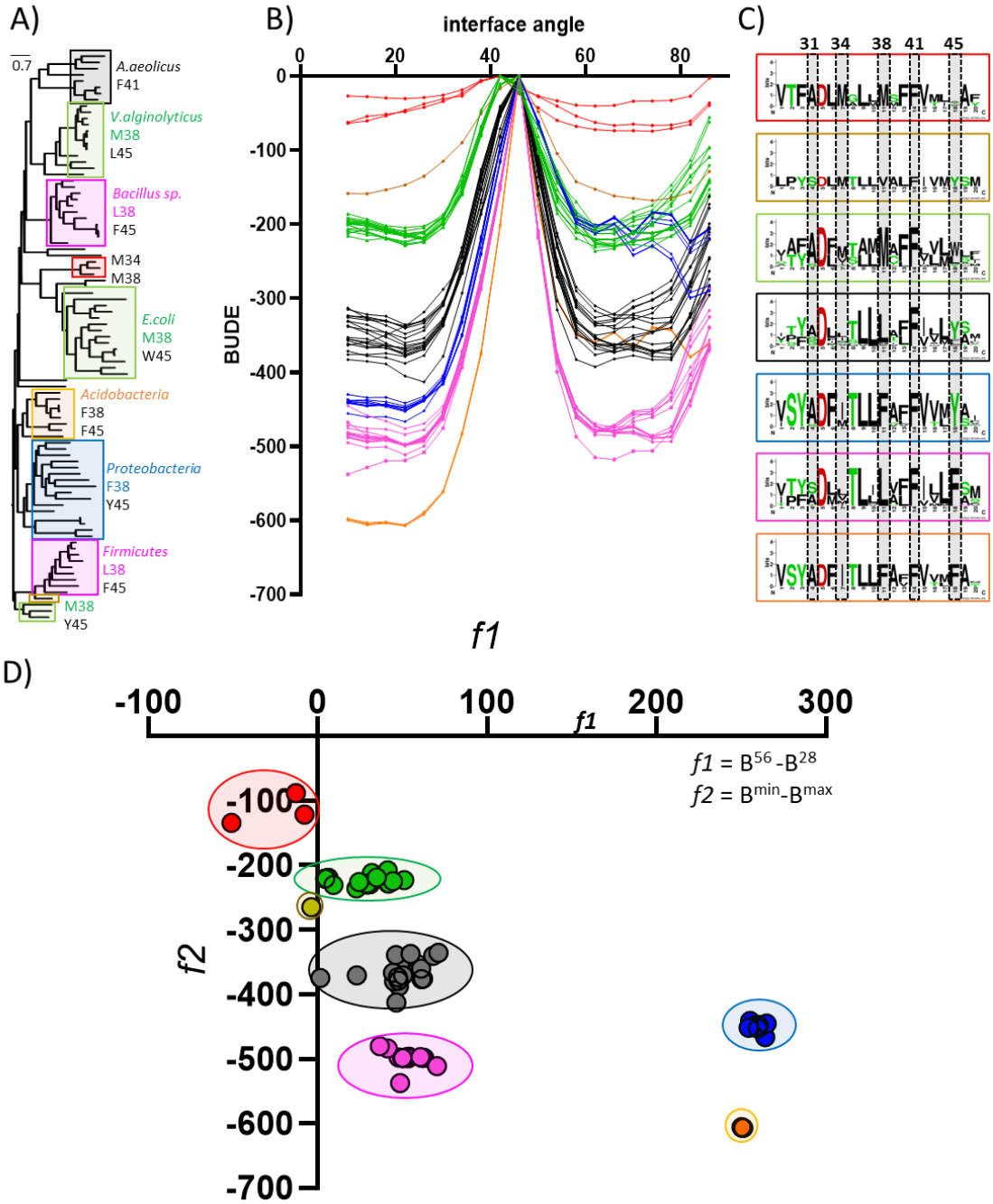


**Figure 4. BUDE analysis of extant MotB sequences.**

A) Phylogeny of extant, full-length MotBs. Clades are labelled by colored boxes corresponding to the clusters highligted in B. A representative member of each clade, or representative bacterial phylum, are shown next to each box. The conserved amino acids indicative of each clade are shown next to each box and numbered according to *E.coli* residues. A detailed phylogeny is provided in SI Figure 10.

B) 2D BUDE plots of extant WT MotB variants, translated by their $BUDE^{max}$ values.
C) Consensus logos for each plot in A. Each logo is inscribed in a box matching the colour of its respective plots in A. Knob-in-hole residues at positions homologous to *Ec*MotB 31, 34, 38, 41 and 45 are highlighted in vertical grey boxes.
D) Graphical representation of the clustered populations of extant MotB stators plotted on a XY graph where X = *f1* and Y = *f2.* The formulas used to calculate *f1* and *f2* for each homolog are provided below the X axis.

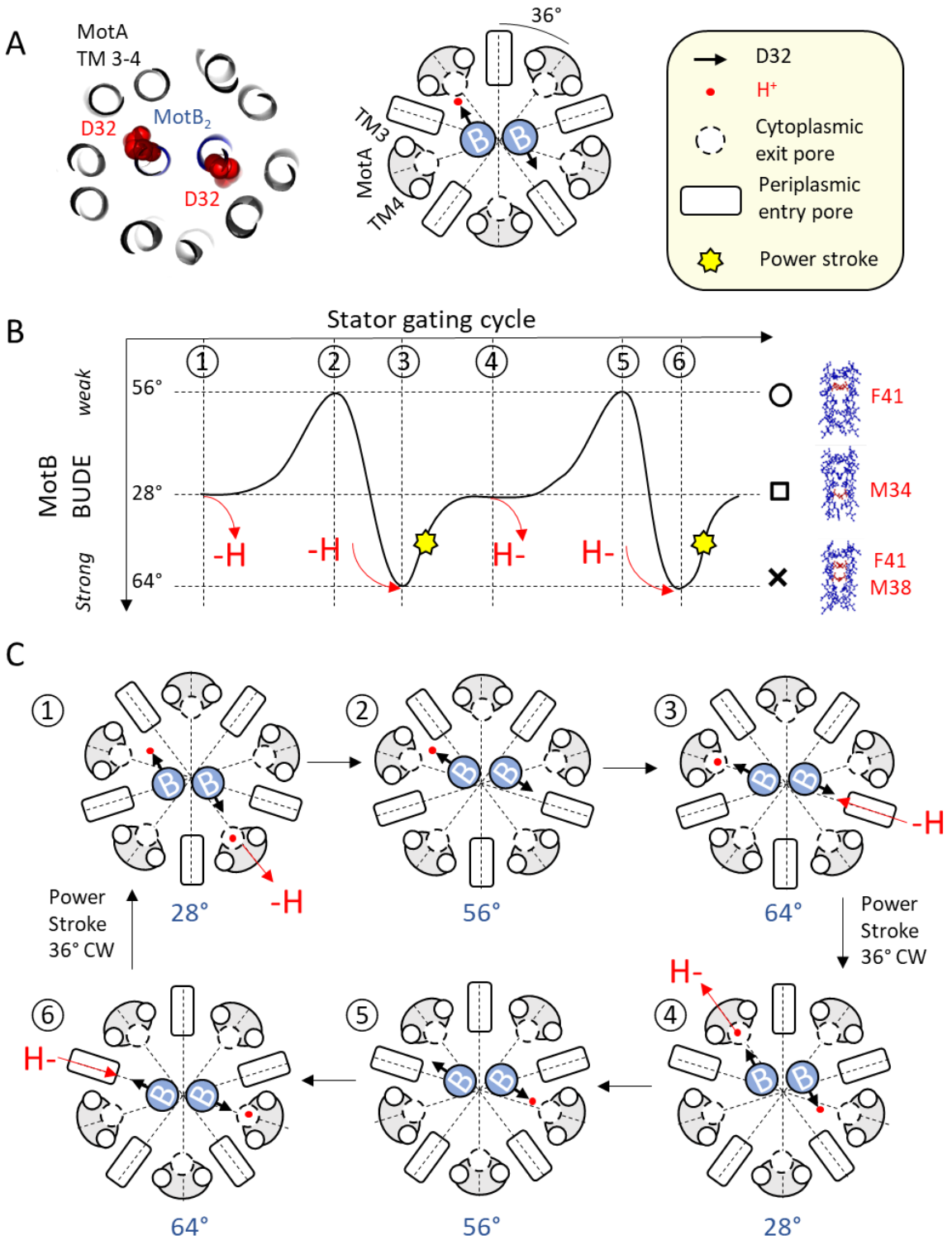


**Figure 5. Rotary model showing the role of MotB coiled-coil conformations in the mechanochemical cycle of the stator complex.**

A) Section of the *Bs*MotAB [PDB 6YSL] structure highlighting the central MotB dimer (blue) and transmembrane helices TM3 and TM4 of MotA (grey) interfacing the MotB dimer. A sphere model (red) indicates the position and orientation of the catalytic aspartate in MotB. A cartoon representation of the crystal structure and

legend detailing each the relevant features of the stator are shown on the right. The dashed lines below separate the stator cross-section in ten identical 36° sectors.

B) Energetic model of the MotB cycle between three stable configurations and the change in BUDE interaction energy at the TM coiled-coil during the gating cycle of the stator. The red arrow indicate binding or unbinding of an $H^+$ or $H_3O^+$ ion at the left or right aspartate (H- or –H, respectively). A yellow star indicates the power stroke and 36° clock-wise rotation of the MotA pentamer around the MotB dimer. Configuration symbols and representative KIH interactions are also shown on the right of the energetic model.

C) Six stages of the mechanochemical cycle model described in B. 1. A proton is trasferred into the cytoplasm through an exit pore immediately after a power stroke. This causes a change in the MotB TM configuration, which rotates counter-clockwise 36° from the 28° (1) to the 64° configuration (3), passing through the 56° configuration (2). Upon reaching the 64° configuration, the aspartate on the left subunit engages MotA at the TM3-4 interface in proximity of the cytoplasmic exit pore (3). A proton then enters from the opposite periplasmic entry pore to bind the unbound aspartate causing a conformational change of the coiled-coil and the concomitant rotation of the MotB dimer and MotA pentamer by 36° clockwise (a power stroke). This rotation restores the coiled-coil to the 28° configuration causing the engaged ion to be released into the cytoplasm and the cycle to repeat at the opposite (disengaged) aspartate in (4), (5) and (6) eventually resulting in a new power stroke and the return to stage (1).

## Materials and Methods

### Structural modelling of coiled-coils.

The *B. subtilis* $MotA_5B_2$ structure (PDB:6YSL) (*5*) was used as a reference to model the transmembrane domain of *E. coli* MotB as coiled-coil. We used ISAMBARD to create a specification whereby a parallel dimeric coiled-coil backbone structure could be generated from three parameters: the interface angle, the radius, and the pitch. The coiled-coil backbone structure for the amino acid sequence IAYADFMTAMMAFFLVMWLI (corresponding to the *E. coli* MotB residues 28-47) was optimized using the genetic algorithm evolutionary optimizer from ISAMBARD and SCWRL 4.0 for the optimization of side chain orientations to minimize the total energy of the system as calculated by the BUDE force field. Optimizations were performed using seven different initial interface angle values which corresponded to the seven possible registers of a coiled-coil. The seven optimized coiled-coil models were aligned to the resolved structure of the MotB dimer stalk in PDB structure 6YSL. The alignment revealed that the best initial interface angle that resulted in a good structural match after optimization to the MotB stalk was 51.4°, which corresponds to position *e* for the first residue in the amino acid sequence. The optimized parameter values were 4.54 Å radius, 232.03 Å pitch, and 74.85° interaction angle.

### Calculation of the energy landscapes of the MotB coiled-coils

We used in-house Python scripts to generate a list of 221 sequence variants of the amino acid sequence IAY**A**DF**M**TAM**M**AF**F**LVM**W**LI where residues A31, M34, M38, F41, W45 were systematically mutated to alanine in every permutation; separately the sequence was mutated with isoleucine (for residues A31, M38, and W45), asparagine (for residue M38), and leucine (for residues M34 and F41) in every permutation. These mutations follow coiled-coil design principles to weaken or strengthen dimeric coiled-coils. Finally, additional MotB mutants were added to the list (SI Table 1). For each sequence variant, we used ISAMBARD to generate coiled-coil backbone structural models with radii values ranging from 4 to 6 Å (in 0.1 Å increments) and interface angle values ranging from 10 to 86° (in 4° increments). The pitch was kept constant to a value of to 150 Å. These ranges of values encompass the optimized parameters that best matched the reference structures. The sidechain orientations were optimised using SCWRL 4.0 as part of the ISAMBARD script. For each conformational variant, the total energy of the system was calculated using the BUDE forcefield. The three-dimensional data sets (BUDE total energy as a function of interface angle and radius) were plotted as heatmaps using in-house Python scripts and Matplotlib library. Two-dimensional datasets were generated by integrating the total energy values for a subset of the radii values (4 to 5 Å) which contained the stability wells and instability peaks of interest. The integrated total energy values were plotted as a function of the interface angles. In some analyses, we focused on four regions in the three-dimensional dataset for comparison of the sequence variants (centred on list combinations of radii and interface angles) and a representative energy value for each of the four regions was calculated by averaging two neighbouring points from the two-dimensional dataset (see Fig. 2C).

### *E. coli* strains, plasmids, and culture media

*E. coli* strain RP437 Δ*motAB* was prepared using the No-Scar method[29]. MotA and MotB were expressed from plasmid pDB108 ($Cm^+$) after induction with 0.1 mM Arabinose. FliC-sticky *E. coli* RP437 cells (Δ*motAB* Δ*cheY* Δ*pilA fliC*$^{st}$) (*6*) were used to perform the tethered cell assay experiments. Liquid cell culturing was done using LB broth (85 mM NaCl, 0.5% yeast extract, and 1% Bacto tryptone). Point mutations in *motB* on the pDB108 plasmid were generated using the QuikChange™ technique and verified by Sanger sequencing. A list of primers used is provided in Supplementary Table 2. Cells were cultured on agar plates composed of LB broth and 1% Bacto agar (BD Biosciences, U.S.A.). Swim plate cultures were performed on the same substrates adjusted for agar content (0.3% Bacto agar).

### Single cell swimming assay and tethered cell assay.

Free-swimming cells were grown overnight in TB buffer (85 mM NaCl, 1% Bacto tryptone) at 30°C to $OD_{600}$ of ~0.5 then washed three times in 1 ml MB buffer (85 mM NaCl and 10 mM KPi, pH=7.0) before resuspension in 500 µl of MB buffer and imaging in a tunnel slide. The tethered cell assay was performed as previously described (*7*). Briefly, 1 ml of cells [optical density at 600 nm (OD600) = 0.5] grown in TB buffer was sheared by passing the cell suspension through a 26-gauge syringe needle 30 times. These cells were then washed three times in 1 ml MB and lastly resuspended in 500 µl of the same buffer. Then, 20 µL of suspension was loaded into a tunnel slide prefilled with MB buffer and incubated for 10 min at room temperature. The unbound cells were then removed from the tunnel slide by washing with a total of 200 µl of MB buffer (~10 times the tunnel slide volume) and then loaded onto a phase contrast microscope for video recording. Time-lapse videos were recorded at 40x magnification on a phase contrast microscope (Nikon). Time-lapse videos were collected using a camera (Chameleon3 CM3, Point Grey Research) recording 20-s-long videos at 20 frames/s. Experiments involving single-cell tracking were recorded at 60 frames/s. A custom LabView software (*7-9*) was used as previously reported to estimate specific rotational parameters of the tethered cells such as rotation frequency (speed), clockwise and counterclockwise bias, switching frequency, and speed of swimming cells.

**REFERENCES**


1. Nakamura, S., and Minamino, T. (2019). Flagella-driven motility of bacteria. Biomolecules *9*, 279. 10.3390/biom9070279.

2. Mondino, S., San Martin, F., and Buschiazzo, A. (2022). 3D cryo-EM imaging of bacterial flagella: Novel structural and mechanistic insights into cell motility. Journal of Biological Chemistry *298*, 102105. 10.1016/j.jbc.2022.102105.

3. Nirody, J.A., Sun, Y.-R., and Lo, C.-J. (2017). The biophysicist's guide to the bacterial flagellar motor. Advances in Physics: X *2*, 324–343. 10.1080/23746149.2017.1289120.

4. Mandadapu, K.K., Nirody, J.A., Berry, R.M., and Oster, G. (2015). Mechanics of torque generation in the bacterial flagellar motor. Proc Natl Acad Sci USA *112*, E4381–E4389. 10.1073/pnas.1501734112.

5. Guo, S., and Liu, J. (2022). The Bacterial Flagellar Motor: Insights Into Torque Generation, Rotational Switching, and Mechanosensing. Frontiers in Microbiology *13*.

6. Hu, H., Santiveri, M., Wadhwa, N., Berg, H.C., Erhardt, M., and Taylor, N.M.I. (2022). Structural basis of torque generation in the bi-directional bacterial flagellar motor. Trends in Biochemical Sciences *47*, 160–172. 10.1016/j.tibs.2021.06.005.

7. Santiveri, M., Roa-Eguiara, A., Kühne, C., Wadhwa, N., Hu, H., Berg, H.C., Erhardt, M., and Taylor, N.M.I. (2020). Structure and Function of Stator Units of the Bacterial Flagellar Motor. Cell *183*, 244-257.e16. 10.1016/j.cell.2020.08.016.

8. Deme, J.C., Johnson, S., Vickery, O., Muellbauer, A., Monkhouse, H., Griffiths, T., James, R.H., Berks, B.C., Coulton, J.W., Stansfeld, P.J., et al. (2020). Structures of the stator complex that drives rotation of the bacterial flagellum. Nature Microbiology, 1–12. 10.1038/s41564-020-0788-8.

9. Hu, H., Popp, P.F., Santiveri, M., Roa-Eguiara, A., Yan, Y., Liu, Z., Wadhwa, N., Wang, Y., Erhardt, M., and Taylor, N.M.I. (2022). Mechanisms of ion selectivity and rotor coupling in the bacterial flagellar sodium-driven stator unit. 2022.11.25.517900. 10.1101/2022.11.25.517900.

10. Rieu, M., Krutyholowa, R., Taylor, N.M.I., and Berry, R.M. (2022). A new class of biological ion-driven rotary molecular motors with 5:2 symmetry. Frontiers in Microbiology *13*.

11. Sharp, L.L., Zhou, J., and Blair, D.F. (1995). Tryptophan-scanning mutagenesis of MotB, an integral membrane protein essential for flagellar rotation in Escherichia coli. Biochemistry *34*, 9166–9171. 10.1021/bi00028a028.

12. Zhang, X.Y.-Z., Goemaere, E.L., Seddiki, N., Célia, H., Gavioli, M., Cascales, E., and Lloubes, R. (2011). Mapping the interactions between *Escherichia coli* TolQ transmembrane segments. J. Biol. Chem. *286*, 11756–11764. 10.1074/jbc.M110.192773.

13. Lupas, A.N., and Bassler, J. (2017). Coiled Coils – A Model System for the 21st Century. Trends in Biochemical Sciences *42*, 130–140. 10.1016/j.tibs.2016.10.007.

14. Fletcher, J.M., Boyle, A.L., Bruning, M., Bartlett, G.J., Vincent, T.L., Zaccai, N.R., Armstrong, C.T., Bromley, E.H.C., Booth, P.J., Brady, R.L., et al. (2012). A Basis Set of *de Novo* Coiled-Coil Peptide Oligomers for Rational Protein Design and Synthetic Biology. ACS Synth. Biol. *1*, 240–250. 10.1021/sb300028q.

15. Crick, F.H.C. (1953). The Fourier transform of a coiled-coil. Acta Cryst *6*, 685–689. 10.1107/S0365110X53001952.

16. McIntosh-Smith, S., Price, J., Sessions, R.B., and Ibarra, A.A. (2015). High performance *in silico* virtual drug screening on many-core processors. The International Journal of High Performance Computing Applications *29*, 119–134. 10.1177/1094342014528252.

17. Wood, C.W., Bruning, M., Ibarra, A.Á., Bartlett, G.J., Thomson, A.R., Sessions, R.B., Brady, R.L., and Woolfson, D.N. (2014). CCBuilder: an interactive web-based tool for building, designing and assessing coiled-coil protein assemblies. Bioinformatics *30*, 3029–3035. 10.1093/bioinformatics/btu502.

18. Wood, C.W., and Woolfson, D.N. (2018). CCBuilder 2.0: Powerful and accessible coiled-coil modeling: Powerful and Accessible Coiled-Coil Modeling. Protein Science *27*, 103–111. 10.1002/pro.3279.

19. Braun, T.F., and Blair, D.F. (2001). Targeted disulfide cross-linking of the MotB protein of Escherichia coli: evidence for two H(+) channels in the stator Complex. Biochemistry *40*, 13051–13059. 10.1021/bi011264g.

20. Choi, J., Park, H., and Seok, C. (2011). How does a registry change in dynein's coiled-coil stalk drive binding of dynein to microtubules. Biochemistry *50*, 7629–7636. 10.1021/bi200834k.

21. Noell, C.R., Loh, J.Y., Debler, E.W., Loftus, K.M., Cui, H., Russ, B.B., Zhang, K., Goyal, P., and Solmaz, S.R. (2019). Role of Coiled-Coil Registry Shifts in the Activation of Human Bicaudal D2 for Dynein Recruitment upon Cargo Binding. J. Phys. Chem. Lett. *10*, 4362–4367. 10.1021/acs.jpclett.9b01865.

22. Snoberger, A., Brettrager, E.J., and Smith, D.M. (2018). Conformational switching in the coiled-coil domains of a proteasomal ATPase regulates substrate processing. Nat Commun *9*, 2374. 10.1038/s41467-018-04731-6.

23. Stamatakis, A. (2014). RAxML version 8: a tool for phylogenetic analysis and post-analysis of large phylogenies. Bioinformatics *30*, 1312–1313. 10.1093/bioinformatics/btu033.

24. Nishino, Y., Onoue, Y., Kojima, S., and Homma, M. (2015). Functional chimeras of flagellar stator proteins between E. coli MotB and Vibrio PomB at the periplasmic region in Vibrio or E. coli. Microbiologyopen *4*, 323–331. 10.1002/mbo3.240.

25. Islam, M.I., Lin, A., Lai, Y.-W., Matzke, N.J., and Baker, M.A.B. (2020). Ancestral Sequence Reconstructions of MotB Are Proton-Motile and Require MotA for Motility. Front. Microbiol. *11*. 10.3389/fmicb.2020.625837.

26. Beeby, M., Ferreira, J.L., Tripp, P., Albers, S.-V., and Mitchell, D.R. (2020). Propulsive nanomachines: the convergent evolution of archaella, flagella and cilia. FEMS Microbiology Reviews *44*, 253–304. 10.1093/femsre/fuaa006.

27. Beeby, M., Ribardo, D.A., Brennan, C.A., Ruby, E.G., Jensen, G.J., Hendrixson, D.R., and Hultgren, S.J. (2016). Diverse high-torque bacterial flagellar motors assemble wider stator rings using a conserved protein scaffold. Proceedings of the National Academy of Sciences of the United States of America *113*, E1917–E1926. 10.1073/pnas.1518952113.

28. Carroll, B.L., and Liu, J. (2020). Structural Conservation and Adaptation of the Bacterial Flagella Motor. Biomolecules *10*, 1492. 10.3390/biom10111492.

29. Reisch, C.R., and Prather, K.L.J. (2015). The no-SCAR (Scarless Cas9 Assisted Recombineering) system for genome editing in Escherichia coli. Sci Rep *5*, 15096. 10.1038/srep15096.